Hydrogeochemistry, stable isotope geochemistry and geothermometry of CO_2-bearing hydrothermal springs from Western Iran: Evidence for their origin, evolution and spatio-temporal variations

Zahra, Mohammadi[a], Orlando Vaselli[b], Philippe Muchez[a], Claes Hannes[c], Enrico Capezzuoli[b], and Rudy Swennen[a]

[a] Department of Earth and Environmental Sciences, KU Leuven, Celestijnenlaan 200E, Leuven B-3001, Belgium

[b] Department of Earth Sciences, University of Florence, Florence, Italy

[c] Clay and Interface Mineralogy (CIM), RWTH Aachen University, Aachen, Germany

*email: zahra.mohammadi@kuleuven.be

Keywords: Hydrothermal spring, geochemistry, geothermometry, stable isotope, Iran

Abstract

This study aims to hydrochemically characterise three CO_2-bearing springs representing distinct hydrofacies in NW Gorveh (western Iran) and interpret them in the light of their geological setting. The results of laboratory measurements of elemental concentrations, stable oxygen, carbon and hydrogen isotopes, dissolved and particulate organic and inorganic carbon (DIC, DOC, POC, PIC) and alkalinity are combined with in situ measurements of pH and temperature. Parameters such as alkalinity, DIC, Ca^{2+} and pCO_2 concentration display a strong, positively correlated values, with systematic decrease from the spring vent in down-flow direction for the three spring systems. The inverse correlation of pH and $\delta^{13}C_{DIC}$ is caused by CO_2 degassing. The $\delta^{18}O$ and δD values show no significant variation, related to minor or no evaporation due to normal ambient temperatures. The low concentration of POC and PIC and DOC compared to that of DIC and the lack of correlation between them reflects predominant inorganic carbon in these fluids.

Spring I is oversaturated in calcite with additional dissolution of CO_2, and despite high concentrations of Na^+ and Cl^-, undersaturated in halite, indicating a fluid of geothermal origin and/or reflecting steady state dissolution. This is related to water-rock interaction processes with carbonate and evaporitic rocks,

that affected the isotopic signature of $\delta^{18}O$, which is shifted to the right of the global meteoric water line. Spring I also represents a partially equilibrated and mature (deep) chloride type water. Spring II and III are less saline and represent a different fluid circulation and/or reflecting shorter residence time. The two latter springs are characterised by peripheral (shallow) dilute chloride-bicarbonate type waters. Decreasing key parameters especially in Spring III during the winter suggest that superficial mixing with rain and meteoric water results in high temporal variations. Cation and stable carbon isotope geothermometry applied to the studied springs reveal an average reservoir temperature of ~210, 110 and 90 °C for Spring I and II and III, respectively. The geochemical and isotopic data allowed to depict a conceptual model where the hydrothermal reservoir for Spring I is residing in carbonate and evaporitic rocks (most likely the Qom Formation) situated at a depth of 3-4 km whereas those of Spring II and III are likely sourced from a shallower depth (1-2 km) in correspondence with carbonate and porous and permeable volcanic rocks.

Integration of hydrofacies with conceptual hydrological and geological models forms the base towards a proper understanding of water circulation patterns, increasingly important for sustainable water management and geothermal applications.

1. Introduction

Due to changes in climate, Iran is experiencing unprecedented changes like drying of lakes and rivers, droughts and floods (Vaghefi et al., 2019). This is in line with the worldwide growing prevalence of droughts and increasing number of water-stressed areas (e.g. UNICEF, 2019; WHO, 2019). Sustainable water management is becoming increasingly important, especially in (semi-)arid areas like Iran. In addition to exploitation for drinking water and agricultural irrigation, investigations on deep circulation of meteoric water forming hydrothermal systems are gaining interest since they play a significant role in ore deposits and geothermal applications (e.g. Nicholson, 1993; Chandrajith et al., 2013; Pérez-Zárate et al., 2015).

All these applications require a proper hydrogeological and hydrochemical understanding. Alongside with tectonic and hydrological modelling, hydrochemical spring characterization provides crucial

insights into fluid-rock interaction processes, origin of waters, reservoir depth and temperature (e.g. Giggenbach and Glover, 1992). Considerable research has been devoted to address the elemental composition and isotope characteristics of hydrothermal waters and related inorganic carbonate deposits (e.g. Fouke et al., 2000 and 2011; Liu et al., 2003; Grasby et al., 2003; Pentecost, 2005; Veysey et al., 2008; Capezzuoli et al., 2009; Linares et al., 2009; Jones and Renaut, 2010; Keppel et al., 2011; Acikel and Ekmekci, 2016; Alçiçek et al., 2019). Nevertheless, similar studies in Iran are still rather scarce (Keshavarzi et al., 2011; Ebrahimi et al., 2019).

Thermal springs are characterized by variable chemical compositions related to differences in their hydrogeology. This can be reflected by significant differences in the adjacent related travertine morphologies and textures (e.g. Mohammadi et al., 2019). Travertine is a chemical sedimentary deposit precipitating from $CaCO_3$-oversaturated waters due to CO_2 degassing (Ford and Pedley, 1996; Pentecost, 2005; Liu et al., 2010). These aforementioned carbonate rock types often have a cultural, tourist and ecological importance (Keppel et al., 2012). However, they are also used as proxies of past hydrothermal fluid activity (e.g. Brogi et al., 2016 and 2017; Teboul et al., 2016; Vignaroli et al., 2016., Mohammadi et al., 2020; Claes et al., 2019). Depending on the precipitation conditions and fluid chemistry, determined by the interplay of geo-hydrology, tectonics and climate, travertine systems may form and evolve differently (e.g. Pentecost, 2005). The widely applicable fundamental tools for studying thermal waters include regional scale hydraulics, water chemistry, δD and $\delta^{18}O$ water composition and geothermometry (Yang et al., 2017).

Consequently, a hydrochemical characterization of three adjacent, though different, hydrothermal springs was carried out. These measurements include chemical composition, stable isotope ratios of water (δD and $\delta^{18}O$), alkalinity concentration together with the stable isotope composition of particulate organic/inorganic carbon (POC/PIC) and dissolved organic/inorganic carbon (DOC/DIC) along several stations downstream from the orifice. Information on the travertines adjacent to the present-day springs is available from parallel research (Mohammadi et al., 2019), to get a better understanding of the fluid composition in space and time. Besides the (i) hydrochemical characterization of the three springs, this

study aims to define (ii) their origin, evolution and reservoir temperature and (iii) spatial and seasonal variations after upwelling at the surface from orifice and along the down-flow trajectory.

2. Geological setting

The Hamadan-Tabriz belt (HTV) is part of the W-NW oriented magmatic-metamorphic belt of the Sanandaj–Sirjan geological zone. This zone formed between the Arabian and Eurasian plates along the Turkish-Iranian plateau (e.g. Allen et al., 2013) and was defined as a fault and thrust zone, where different slices of metamorphosed and non-metamorphosed Phanerozoic units of the Afro-Arabian passive continental margin overthrusted, along with obducted ophiolites (Alavi, 2004). The lithology includes sedimentary, metamorphic and igneous rocks. The oldest known rocks consist of Triassic–Jurassic volcano-sedimentary metamorphosed rocks consisting of black schists, meta-andesites, amphibolites, metagabbros, marbles, micaschists, phyllites, dark green sandy shales and slates (Karimi Nezhad et al., 2014). The Tertiary sedimentary-igneous rocks include tuffs, lapilly tuffs, pumiceous tuffs, argillaceous limestones, silicate, latites and dacites. The younger lithologic units include Quaternary andesitic basalt to alkali basalt, travertine deposits, basanites, poorly-consolidated conglomerates and alluvium terraces and fans (Karimi Nezhad et al., 2014). Quaternary volcanism accompanied strike-slip-related transtensional deformation along faults in the HTV belt segment of the Sanandaj–Sirjan fault zone (GSI, 1999). According to Boccaletti et al. (1976), there are two distinct volcanic cycles in the HTV belt. The first one (Late Miocene), produced high-K calc-alkaline volcanic rocks (dacitic and rhyolitic domes), which were interpreted as the final products of the calc-alkaline Tertiary deformation phase in central Iran. The second volcanic cycle (mostly of Pleistocene age: 0.5–1.3 Ma) consists of undersaturated, mainly potassic, alkaline products (rhyolitic domes). The widespread travertine deposits form one of the common Quaternary deposits in this belt which in some places are presently active. In spite of the extensive investigations carried out on the volcanic rocks of this region, not much attention was paid to the travertine deposits.

The study area, where the three studied springs within the Babagorgor watershed occur, is situated between 47°32′ and 48°11′ E and 35°05′ and 35°30′ N. It is located 6 km N of Ghorveh county in the

district of Kurdistan, western Iran (Fig. 1). This area is characterized by a Mediterranean climate with cold, rainy and snowy winters, and warm summers with an average annual rainfall of 480 mm and an average annual temperature of 6.1 °C (for the period 1993 to 2014 at Ghorveh Station; Karimi Nezhad et al., 2014).

The three main springs that were investigated occur nearby presently active as well as impressive paleo-travertine deposits. Spring I occurs adjacent to a paleo-fissure ridge where sparitic fabrics dominated, Spring II discharges near a paleo- mound travertine while Spring III is situated along a stream channel with several feeders, which tend to form horizontal travertines. It should be noted that the two last springs dominated by micritic fabrics. Spring I is located within a dome shaped structure (2 m high) with a diameter of 1 m and, water depth $\leq$ 0.5 m (Fig. 2A). The related travertines possess a sparitic fabric (Mohammadi et al., 2019). Spring II discharges from a 20 m high structure and a diameter of $\geq$15 m whose depth is not known (Fig. 2B). The deposits that are forming from this water reveal mainly micritic fabrics (Mohammadi et al., 2019). Spring III consists of several feeders that emerge along a channel (4 m wide) with 2 m high overbanks, and water depth between 0.4 and 0.8 m (Fig. 2C). Moreover, along the Spring III canal intercalations of travertine/tufa and clay, which are relatively unconsolidated, occur. Relatively vigorous gas bubbling, related to a CO_2-rich gas discharge, also occurs in each of three springs where a persistent smell of rotten eggs suggests the presence of hydrogen sulfide. In addition to the spring waters and waters collected down-stream, fresh water samples were collected from springs around Delbaran city (being the closest city within the Babagorgor watershed) and from a well near Galsnan village, which supplies drinking water to the city of Delbaran. An additional sample, named Ali Sadr, was collected from the homonymous cave, which is the world's largest water cave, located in the mountain surrounding Gorveh (north of Hamadan) in the HTV belt.

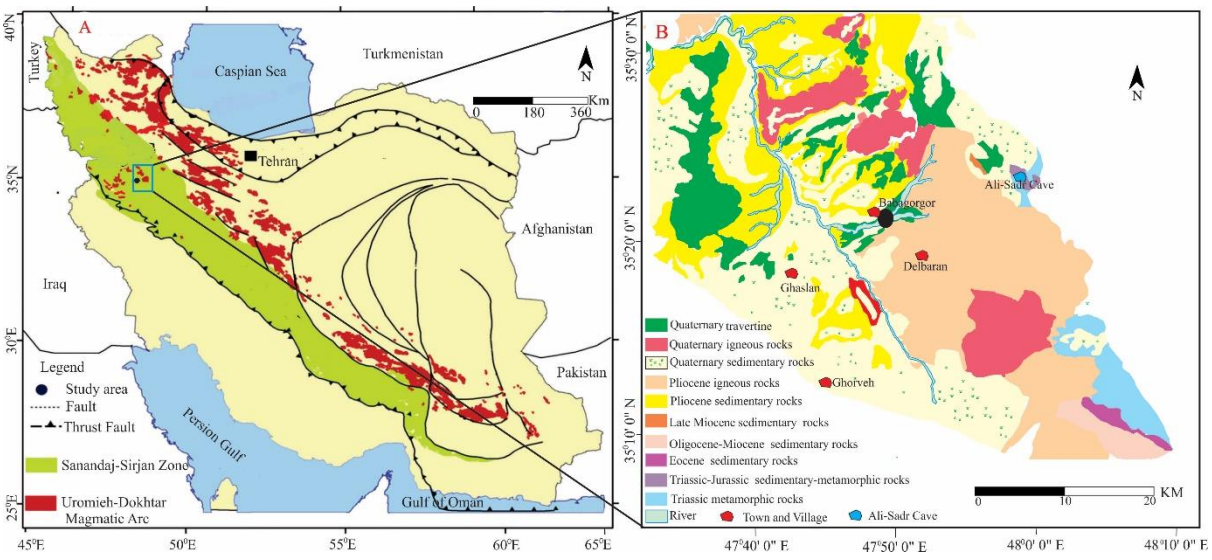


Fig. 1. A) Map of Iran with indication of the study area (blue rectangle) modified from Sahandi et al. (2005). B) Geological map of the study area (modified from the Geological Survey of Iran and Karimi Nezhad et al., 2014). The black circle is the study area.

3. Material and methods

3.1. Field sampling and laboratory analysis

The three selected springs were sampled along their stream pathways in August 2017 and January 2018. In the field, pH and water temperature were measured with a portable probe, Cond340i. The Spring I was discharging from a small pipe (Fig. 2A) with a relatively low discharge rate, i.e. about 1L/sec in both seasons. The discharge rate of Spring II was higher than Spring I, about 20L/sec in both seasons. In spite of the low discharge rate of Spring III, water feeders emerging along the channel (Fig. 2C and D) were able to produce a relatively high discharge rate of about 15L/sec in summer and three times higher in winter due to direct meteoric water (rain) infiltration. Due to the input of meteoric water in winter, much higher flow rates were observed along the channel of Spring III, whereas those of the other two springs remained rather constant.

Water samples were collected from the orifice and along the downstream trajectory at 4 sites for Spring I, 5 sites for Spring II and 7 sites for Spring III (Fig. 2E). The water samples were filtered with 0.45 µm membranes in the field before being transferred to two pre-washed polyethylene bottles. The aliquots

for main and trace species were acidified with ultrapure HNO_3. Major cations (Ca^{2+}, Na^{+}, K^{+}, Mg^{2+}, Si^{4+}) and trace elements (e.g. Li, B, As, Sr, Rb and Ba) were analyzed using inductively coupled plasma optical emission spectrometry (ICP-OES) (KU- Leuven and Florence University). Major anions (Cl^{-}, SO_4^{2-} and Br^{-}) were analyzed by ion chromatography with a Dionex IC2000 equipped with an AS18 column (KU Leuven and Florence University). The analytical error of the main cations and anions was <3% while that of trace elements was <10%.

Total alkalinity (TA) was measured by open-cell titration with HCl 0.1 mol L^{-1} (Gran, 1952) on 50 mL of water. The analytical data were quality checked with a certified reference material obtained from Andrew Dickinson (Scripps Institution of Oceanography, University of California, San Diego, USA). Typical reproducibility of TA measurements was better than ± 3 µmol L^{-1}.

Particulate organic and inorganic carbon (POC and PIC) contents and the isotope composition of POC ($\delta^{13}C_{POC}$) were obtained by filtering 50–100 mL of water on pre-combusted (overnight at 450 °C) glass fiber filters (25 mm GF/F, 0.7 µm nominal pore size). The filtrate was further filtered with 0.2 µm polyethersulfone syringe filters for DOC content and $\delta^{13}C_{DOC}$ analysis (stored in 40 mL glass vials with polytetrafluoroethylene coated septa with 50 µl H_3PO_4).

Filters for POC and $\delta^{13}C_{POC}$ were decarbonated with HCl flumes for 4 h, re-dried and packed in Ag cups prior the analysis on an elemental analyzer – isotopic ratio mass spectrometer EA-IRMS (Thermo EA1110 with Thermo DeltaV Advantage). Calibration of POC and $\delta^{13}C_{POC}$ measurements were performed with IAEA-600 (caffeine), and two internal (Leucine and Tuna tissue) standards.

Samples for dissolved organic carbon (DOC) concentration and $\delta^{13}C_{DOC}$ were filtered through pre-flushed 0.2 µm syringe filters, kept in 40mL borosilicate vials with Teflon-coated screw caps and preserved with 100 µL of H_3PO_4 (50 %). Analysis for DOC concentrations and $\delta^{13}C_{DOC}$ were performed with an IO Analytical Aurora 1030W coupled to an IRMS (Thermo delta V Advantage). Typical precision observed in duplicate samples was in 95% cases ± 5‰ for DOC and ± 0.2‰ for $\delta^{13}C_{DOC}$. Quantification and calibration were performed with a series of standards prepared in different

concentrations, using both IAEA-C6 ($\delta^{13}C$ = - 10.4‰) and internal sucrose standards ($\delta^{13}C$ = - 26.9‰ ± 0.04).

Samples for stable C isotopic composition of dissolved inorganic carbon ($\delta^{13}C_{DIC}$) were collected by filling 12 mL headspace vials (Labco Exetainer) without bubbles. 20 µL of a saturated $HgCl_2$ solution was added for sample preservation. Then, 2mL helium headspace was created, and 100 µL of phosphoric acid (H_3PO_4 99 %) was added in order to convert all inorganic C species to CO_2 before measuring the $\delta^{13}C_{DIC}$. After overnight equilibration at 25.0 ± 0.1 °C, 200 µL of gas were injected with a gastight syringe into the abovementioned EA-IRMS. The obtained data were corrected for isotopic equilibration between dissolved and gaseous CO_2 as described in Gillikin and Bouillon (2007). Calibration of the $\delta^{13}C_{DIC}$ measurement was performed with the international certified standards NBS-19 and LSVEC. The reproducibility of $\delta^{13}C_{DIC}$ measurement was typically better than ± 0.2 ‰.
Dissolved inorganic carbon (DIC) concentrations were calculated from the pCO_2 and TA measurements (taking water temperature into account) by solving inorganic carbon system equations using dissociation constants from Mehrbach et al. (1973). The CO_2-excess, defined as the quantity of DIC theoretically transferred as CO_2 to the atmosphere after water–air equilibration, was calculated as the difference between the measured DIC and a theoretical DIC at atmospheric equilibrium.

A syringe-headspace technique (Kratz et al., 1997; Teodoru et al., 2009) was used in the field for the determination of pCO_2. 30 mL of atmospheric air was equilibrated with 30 mL of water by vigorously shaking for 5–10 min in four replicate gas-tight syringes. 30 mL of equilibrated gas and a sample of atmospheric air were then injected in an IR gas analyzer (Li-Cor® models 820 or 840, or PP systems® model EGM-4); the first gas injection served as a purge for the air circuit and cell and the three other injections were used as triplicate pCO_2 determination (average repeatability of ± 1 %).

Samples for $\delta^{18}O$ and δD analysis were collected in 12 mL Labco exetainer vials. For $\delta^{18}O$, samples were measured after equilibration with CO_2 using an Thermo Gas-Bench coupled to a ThermoDelta V Advantage IRMS, and calibrated using 3 in-house standards. For $\delta^{2}H$, 4 replicates per sample were injected in a Thermo Flash EA with a reduced Cr column held at 1030 °C, coupled to a Thermo Delta

V IRMS. Calibrations were performed with 3 in-house standards. The analytical error was ±0.2 and ±1.5 for $\delta^{18}O$ and δD, respectively.

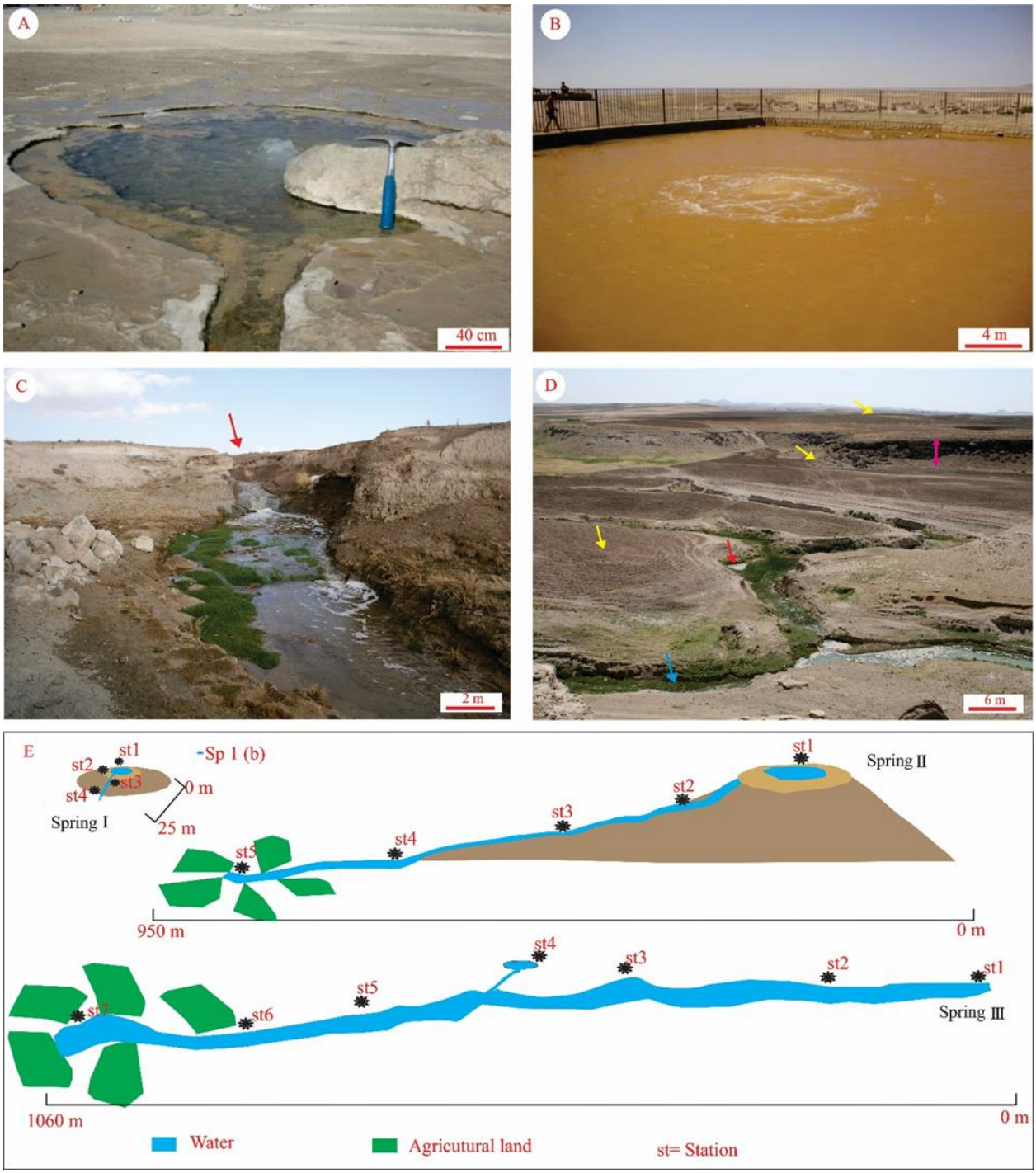


Fig. 2. Spring I (A), Spring II (B) and Spring III (C) with indication of vent (red arrow) (D). In D, the red arrow indicate station 4 along spring III the blue arrow refers to the spring III channel; the yellow

arrows are agricultural land whereas the pink arrow indicates the travertine deposits. (E) Schematic drawing of the three springs; the stars indicate the location from where the water samples were collected.

3.2. Data processing: Saturation index (SI)

The mineral saturation index (SI) was calculated by applying the geochemical code PHREEQCi (Parkhurst and Appelo, 1999). The equilibrium region for minerals is considered to be equal to zero (SI = 0). An SI > 1 reflects oversaturation and mineral precipitation, while SI < 0 reflects undersaturation and mineral dissolution processes.

4. Results

4.1. Main physicochemical data

Spring I had a temperature of 15 °C in both summer and winter. The pH was oscillating between 7.0 (at the orifice) and 8.7 (down-flow). In spite of increasing pH, the temperature maintained relatively constant along the course. Spring II showed a temperature of 20 °C in summer and 18 °C in winter and decreased down to16 °C and 15 °C at the last measuring stations, respectively. The pH was around 7 at the orifice and increased up to 7.8 downstream. In the distinct water discharges feeding Spring III, temperature was varying between 14 °C in summer and 10 °C in winter. The pH was 6.8 at the orifice and 7.5 downstream.

4.2. The chemical and isotopic compositions

The chemical and isotopic compositions were significantly different between Springs I, II and III (Table 1). In particular, Spring I showed high contents of Ca^{2+} (up to 569 mg/L), K^{+} (up to 780 mg/L), and HCO_3^{-} (up to 3,867 mg/L) although the highest concentrations were related to Na^{+} and Cl^{-}, being around 7,148 mg/L and 9,748 mg/L, respectively. Lower contents of Ca^{2+} than that recorded at the orifice of Spring I were measured at Springs II and III (up 250 and up 220 mg/L, respectively) as well as for the other main solutes (Table 1). However, the lowest contents pertained to the waters collected from Ghaslan, Delbaran and Ali Sadr (with temperature and pH values varying between 12 and 14 °C and

6.8 and 6.9, respectively). The Piper diagram for the studied waters is reported in Fig. 3, highlighting that Spring I had a Na-Cl facies signature whereas Spring II and Spring III were Ca(Na)- HCO_3. A Ca-SO_4 composition characterizes the spring waters from Ghaslan, Delbaran and Ali Sadr.

Sample Name	T(°C)	Distance of first step (m)	pH	TDS	SiO_2	HCO_3^-	Cl^-	SO_4^{2-}	Na^+	K^+	Mg^{2+}	Ca^{2+}	Err
Sp I 1 w	15	1	7.2	21397	30	3504	9449	320	6922	592	67	271	0.7
Sp I 2w	14	7	8.3	21725	30	3506	9728	331	7198	610	66	72	-0.8
Sp I 1(b)w	14	30	7.3	23346	28	3446	9291	1975	6983	702	98	569	-0.2
Sp I 1 s	15	1	7.1	22315	30	3866	9702	367	6912	780	89	271	-0.6
Sp I 1(b) s	15	30	7.1	21899	29	3517	9718	437	6924	728	89	199	-0.7
Sp II 1w	20	1	7.0	1998	58	807	292	280	271	30	60	250	4.8
Sp II 2w	17	200	7.0	1758	60	751	252	231	284	31	66	136	2.5
Sp II 3w	15	350	7.2	1666	58	702	247	225	287	31	66	100	1.3
Sp II 4w	15	550	7.6	1717	56	616	290	280	322	30	66	93	1.2
Sp II 1 s	20	1	7.1	2736	60	1414	255	220	426	34	81	260	4.7
Sp II 2 s	18	200	7.2	2208	61	1100	251	225	284	32	60	250	1.4
Sp II 3 s	16	350	7.5	1946	59	898	250	227	391	31	65	76	1.0
Sp II 4 s	16	550	7.6	1935	58	890	259	235	389	31	67	56	-1.3
Sp II 5 s	16	950	7.8	1873	59	829	260	235	393	32	67	51	0.4
Sp III 1 w	11	1	6.8	1945	68	620	460	232	435	21	66	98	2.9
Sp III 2 w	11	160	6.9	1452	71	628	114	305	240	17	47	96	-0.6
Sp III 3 w	11	320	7.1	1437	62	642	116	306	229	19	59	63	-4.3
Sp III 4 w	11	420	6.7	1458	133	722	97	219	138	18	39	220	4.0
Sp III 5 w	11	670	7.1	1755	72	771	130	327	338	17	46	121	4.0
Sp III 6 w	11	870	7.0	1492	64	654	116	310	271	18	58	61	-0.8
Sp III 7 w	11	1060	7.2	1548	65	642	126	313	320	18	52	75	4.2
Sp III 2 s	14	160	6.8	1895	63	1020	132	251	343	22	48	76	-4.9
Sp III 4 s	14	670	7.3	2624	70	1482	220	235	420	28	51	180	-4.8
Sp III 6 s	14	870	7.5	1853	66	908	217	230	346	28	51	68	-4.9
Sp III 7 s	13	1060	7.0	1675	67	807	147	284	280	23	55	73	-4.8
Ghaslan	13	-	6.9	465	6	310	12	24	54	1	15	42	-1.5
Delbaran	14	-	6.9	362	4	193	10	35	25	6	9	52	4.6
Alisadr1	12	-	6.8	293	7	194	6	24	10	2	15	42	-0.1

Table 1. Main chemical composition (in mg/L) of the studied waters. (w=winter samples, s=summer samples and Err= error in the anion and cation imbalance).

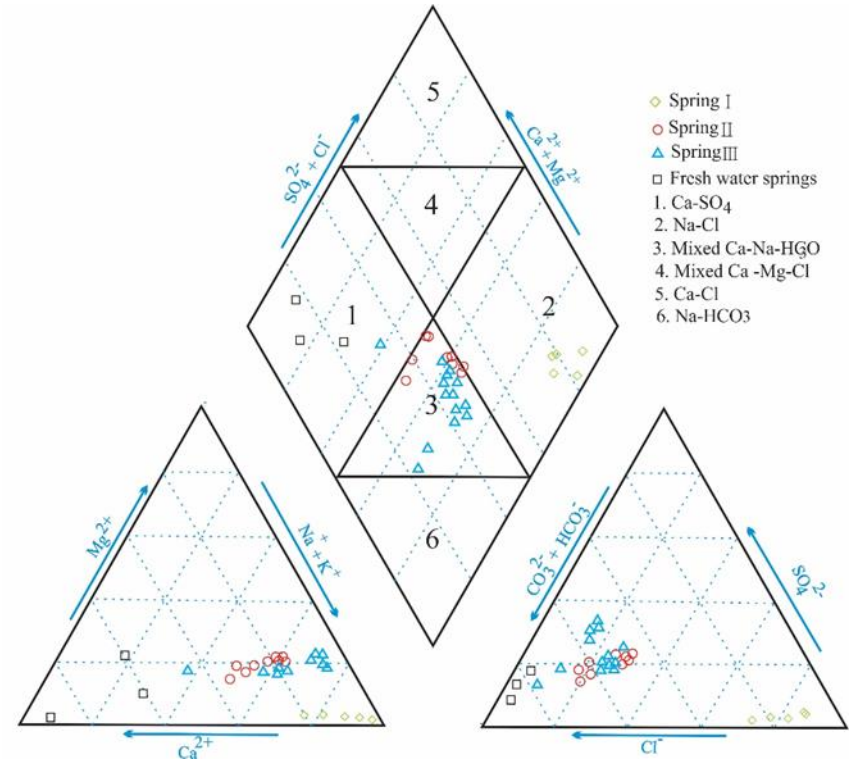


Fig. 3. Piper diagram with position of the studied water samples.

4.3. Trace elements

The high concentrations of trace elements (Li, B, As, Rb, Sr and Ba) mimic those recorded for the main solutes since Spring I has the highest contents (Table 2). The values of the remaining trace elements have extremely low concentrations, even below the instrumental detection limit as shown in Appendix 1. Consequently, they will not be considered in the present study. Lithium, B, Rb, Sr, and Ba at Spring I were up to 39540, 222234, 9442, 6428 and 104 µg/L, respectively, which were at least one order of magnitude higher than those recorded at the orifice of Spring II and Spring III, with the exception of Sr. Notably, Arsenic at Spring I had contents up to 183 µg/L which is comparable with those recorded at Spring III, whereas those at Spring II were up to 76 µg/L. Although Spring II and III showed lower concentrations than those recorded for Spring I they are higher than those determined at Delbaran, Ghaslan and Ali Sadr (Table. 2).

Sample Name	Li	B	As	Rb	Sr	Ba
Sp I 1 w	38380	215296	183	9364	6428	62
Sp I 2w	39540	222234	170	9442	4039	25
Sp I 1(b)w	39170	219669	74	8611	7246	78
Sp I 1 s	34953	220448	167	7141	7717	77
Sp I 1(b) s	33075	203717	71	6219	7707	104
Sp II 1w	600	5593	29	177	2287	18
Sp II 2w	624	4296	37	180	2057	10
Sp II 3w	629	4124	41	183	1822	8
Sp II 4w	630	4057	41	183	1637	6
Sp II 1 s	800	3338	35	176	2461	16
Sp II 2 s	738	3131	54	151	2454	13
Sp II 3 s	664	3954	46	183	827	6
Sp II 4 s	663	4017	64	186	228	3
Sp II 5 s	674	4069	76	187	260	3
Sp III 1 w	96	993	172	-	1675	31
Sp III 2 w	102	1047	178	4.6	1611	32
Sp III 3 w	108	1016	130	5.2	1705	35
Sp III 4 w	163	1034	151	54	2031	83
Sp III 5 w	138	1117	71	9.1	2036	36
Sp III 6 w	131	1133	132	7.2	1773	32
Sp III 7 w	101	973	177	4.1	1597	32
Sp III 2 s	211	1575	19	51	2177	33
Sp III 4 s	543	3468	71	96	2216	23
Sp III 6 s	272	3505	44	62	2211	34
Sp III 7 s	539	1795	67	96	2272	23
Ghaslan	41	301	-	-	324	8
Delbaran	8	122	131	21	664	89
Alisadr1	20	2721	12	6	368	10

Table 2. Trace element concentrations of the water samples from the studied area (µg/L) (w = winter samples, s=summer samples.

4.4. Mineral saturation index (SI)

The mineral saturation indexes (SI) are shown in Table 3. The focus was on calcite, aragonite, dolomite and evaporite minerals (anhydrite, gypsum and halite), as well as quartz and chalcedony as potential contributors to explain the solute concentrations in the analyzed springs. The water is undersaturated regarding the anhydrite, gypsum and halite, whereas it is oversaturated concerning the calcite, and dolomite and in some cases aragonite. However, during winter in Spring III the last three minerals indicate undersaturated to saturated conditions for most minerals.

Sample Name	Aragonite	Calcite	Dolomite	Anhydrite	Gypsum	Halite	Chalcedony	Quartz
Sp I 1w	0.86	1.02	1.65	-1.87	-1.46	-2.95	0.11	0.57
Sp I 2w	1.83	1.99	3.54	-1.88	-1.44	-2.92	0.12	0.59
Sp I 1 (b) w	1.11	1.26	1.92	-0.84	-0.39	-2.96	0.11	0.59
Sp I 1s	0.72	0.87	1.47	-1.81	-1.40	-2.94	0.11	0.57
Sp I 1 (b) s	0.59	0.75	1.36	-1.87	-1.45	-2.94	0.11	0.57
Sp II 1w	0.43	0.58	0.80	-1.32	-0.95	-5.73	0.28	0.73
Sp II 2w	0.09	0.24	0.40	-1.61	-1.22	-5.76	0.32	0.77
Sp II 3w	0.10	0.25	0.54	-1.75	-1.34	-5.76	0.33	0.79
Sp II 4w	0.41	0.56	1.19	-1.70	-1.29	-5.65	0.31	0.77
Sp II 1s	0.72	0.87	1.51	-1.45	-1.09	-5.61	0.28	0.73
Sp II 2s	0.69	0.84	-1.04	-1.42	-5.78	3.24	0.32	0.77
Sp II 3s	0.39	0.54	1.24	-1.87	-1.47	-5.63	0.33	0.79
Sp II 4s	0.32	0.47	1.25	-1.98	-1.58	-5.61	0.31	0.77
Sp II 5s	0.48	0.63	1.60	-2.03	-1.62	-5.61	0.33	0.79
Sp III 1w	-0.43	-0.27	-0.58	-1.80	-1.35	-5.32	0.45	0.93
Sp III 2w	-0.31	-0.16	-0.49	-1.64	-1.18	-6.16	0.48	0.95
Sp III 3w	-0.33	-0.18	-0.23	-1.81	-1.35	-6.17	0.41	0.88
Sp III 4w	-0.09	0.06	-0.48	-1.46	-1.00	-6.48	0.50	0.98
Sp III 5w	0.05	0.20	0.13	-1.55	-1.10	-5.97	0.48	0.95
Sp III 6w	-0.42	-0.27	-0.43	-1.82	-1.36	-6.10	0.42	0.90
Sp III 7w	-0.08	0.07	0.13	-1.76	-1.30	-5.97	0.44	0.91
Sp III 2s	-0.41	-0.26	-0.53	-1.80	-1.37	-6.03	0.39	0.85
Sp III 4s	-0.32	-0.17	-0.28	-1.77	-1.34	-5.99	0.41	0.88
Sp III 6s	0.16	0.31	0.65	-1.86	-1.44	-5.73	0.43	0.89
Sp III 7s	0.18	0.33	0.83	-2.00	-1.57	-5.73	0.40	0.86
Ghaslan	-0.53	-0.38	-1.04	-2.81	-2.38	-7.74	-0.63	-0.17
Delbaran	-0.63	-0.48	-1.54	-2.52	-2.10	-8.15	-0.84	-0.37
Alisadr1	-1.07	-0.91	-2.09	-2.78	-2.34	-8.75	-0.55	-0.08

Table. 3. Saturation indices with respect to selected minerals based on water compositions. (w=winter samples, s=summer samples).

4.5. Spatial and seasonal variations of key hydrochemical parameters in springs

Spatial and seasonal variations were determined by comparing the characteristics of the fluids analyzed from the springs along its downstream trajectory (spatial variation) during warm, dry summer and cold, rainy and snowy winter periods (seasonal variation) (Table 4). The results for both seasons showed a positive correlation between alkalinity, pCO_2, DIC concentration and $\delta^{13}C_{DIC}$ values from the orifice and downstream. DIC concentrations were suffering major changes along the pathways of the three springs in both sampling periods. At the orifices of Springs I, II and III the DIC values were 856, 399 and 435 mg/L, respectively. These values were decreasing downstream down to 759 mg/L at Spring I and 190 mg/L at Spring II and Spring III. However, Spring I showed a rather low decrease at spatial and temporal scale. The DIC concentration decreased in winter for Spring II and Spring III from 210 to

116 (mg/L) and from 165 to 128 (mg/L), respectively. Alkalinity of 3866 mg/L, 1414 mg/L and 1685 mg/L was measured at the emergence of Spring I, II and III, respectively. The latter values gradually decreased to reach 3423 (Spring I), 829 (Spring II) and 807 (Spring III) mg/L in the most distant sampling sites with respect to the orifices. In winter alkalinity value decreases in the Spring II setting from 807 to 616 mg/L, and in the Spring III setting it varies around 650 mg/L. In the Spring I setting, however, not much difference in alkalinity occurs in winter in compression with summer showing 3508 mg/L at first step and 3348 mg/L in the last step at down-flow.

A behavior similar to that of alkalinity and DIC in the three systems is also reflected by pCO_2. Accordingly, the highest amount of pCO_2 corresponded to the orifice of Spring I with 280143 mg/L although comparable values were recorded for Spring II and Spring III (269216 and 205143 mg/L, respectively) (Table 4). In the last sampling location of each site, the following concentrations were measured: Spring I: ~ 223000 mg/L, Spring II: ~ 63200 mg/L and Spring III: ~ 65100 mg/L. pCO_2 significantly decreased in winter from ~ 154,000 to ~ 20,000, from ~ 101000 to ~ 10800 and from ~ 62600 to ~ 8700 mg/L for Spring I, Spring II and Spring III, respectively. It is worth to mention the slight increase in pCO_2 in sampling location 4 in the Spring III. In summer, the $\delta^{13}C_{DIC}$ variation for Spring II and III was characterized by a strong enrichment downstream: from -0.8 to +5 ‰ and from -0.4 to +5.3 ‰ (V-PDB), respectively. For the same period, Spring I showed that the $\delta^{13}C_{DIC}$ values were varying between +3.7 to +5 ‰ (V-PDB) from orifice to the farest sampling site. In winter, the $\delta^{13}C_{DIC}$ values of Spring I and II did not show relevant variations with respect to those registered in summer. Conversely, waters from Spring III indicated that the $\delta^{13}C_{DIC}$ was affected by significant differences in terms of both values and pattern, showing a variation from +4 to +2.1 ‰ from the orifice to the most distal sampling location.

In summer, Spring I had DOC concentrations between 0.8 and 0.5 mg/L from the orifice to the farest sampling location, respectively. Higher DOC contents were recorded for Spring II, being comprised between 6 (at the orifice) and 0.5 (at the most distal site) mg/L. Spring III yielded 2.2 mg/L DOC at the orifice, its concentration clustered around this value along the pathway and reached 3 mg/L at its most

distant sampling location (Table 4).. This parameter in winter varied from 0.4 to 9and 7 to 7.5 mg/L for Spring II and III, respectively, while Spring I showed rather constant concentrations in summer.

The particulate inorganic (PIC) concentration analyzed from filtered samples was ranging from 3.7 to 0.6, from 0.5 to 3mg/L and from 0.2 to 13.6 mg/L for Spring I, Spring II and Spring III, respectively. The particulate organic (POC) concentration from the orifice to the farest sampling point for Spring I was around 2.4 mg/L, whereas those recorded at Spring II and Spring III were varying between 0.6 to 0.7 and 0.3 to 9.1 mg/L, respectively (Appendix 2). The $\delta^{13}C$ isotope values for the three springs were spanning from -26 to -23.6 ‰ for POC and -16.8 and +1.2 ‰ for PIC. As there is no meaningful pattern in both concentration and isotopes of PIC and POC, no in depth discussion can be formulated. The data are shown in Appendix 2.

Sample Name	Aragonite	Calcite	Dolomite	Anhydrite	Gypsum	Halite	Chalcedony	Quartz
Sp I 1w	0.86	1.02	1.65	-1.87	-1.46	-2.95	0.11	0.57
Sp I 2w	1.83	1.99	3.54	-1.88	-1.44	-2.92	0.12	0.59
Sp I 1 (b) w	1.11	1.26	1.92	-0.84	-0.39	-2.96	0.11	0.59
Sp I 1s	0.72	0.87	1.47	-1.81	-1.40	-2.94	0.11	0.57
Sp I 1 (b) s	0.59	0.75	1.36	-1.87	-1.45	-2.94	0.11	0.57
Sp II 1w	0.43	0.58	0.80	-1.32	-0.95	-5.73	0.28	0.73
Sp II 2w	0.09	0.24	0.40	-1.61	-1.22	-5.76	0.32	0.77
Sp II 3w	0.10	0.25	0.54	-1.75	-1.34	-5.76	0.33	0.79
Sp II 4w	0.41	0.56	1.19	-1.70	-1.29	-5.65	0.31	0.77
Sp II 1s	0.72	0.87	1.51	-1.45	-1.09	-5.61	0.28	0.73
Sp II 2s	0.69	0.84	-1.04	-1.42	-5.78	3.24	0.32	0.77
Sp II 3s	0.39	0.54	1.24	-1.87	-1.47	-5.63	0.33	0.79
Sp II 4s	0.32	0.47	1.25	-1.98	-1.58	-5.61	0.31	0.77
Sp II 5s	0.48	0.63	1.60	-2.03	-1.62	-5.61	0.33	0.79
Sp III 1w	-0.43	-0.27	-0.58	-1.80	-1.35	-5.32	0.45	0.93
Sp III 2w	-0.31	-0.16	-0.49	-1.64	-1.18	-6.16	0.48	0.95
Sp III 3w	-0.33	-0.18	-0.23	-1.81	-1.35	-6.17	0.41	0.88
Sp III 4w	-0.09	0.06	-0.48	-1.46	-1.00	-6.48	0.50	0.98
Sp III 5w	0.05	0.20	0.13	-1.55	-1.10	-5.97	0.48	0.95
Sp III 6w	-0.42	-0.27	-0.43	-1.82	-1.36	-6.10	0.42	0.90
Sp III 7w	-0.08	0.07	0.13	-1.76	-1.30	-5.97	0.44	0.91
Sp III 2s	-0.41	-0.26	-0.53	-1.80	-1.37	-6.03	0.39	0.85
Sp III 4s	-0.32	-0.17	-0.28	-1.77	-1.34	-5.99	0.41	0.88
Sp III 6s	0.16	0.31	0.65	-1.86	-1.44	-5.73	0.43	0.89
Sp III 7s	0.18	0.33	0.83	-2.00	-1.57	-5.73	0.40	0.86
Ghaslan	-0.53	-0.38	-1.04	-2.81	-2.38	-7.74	-0.63	-0.17
Delbaran	-0.63	-0.48	-1.54	-2.52	-2.10	-8.15	-0.84	-0.37
Alisadr1	-1.07	-0.91	-2.09	-2.78	-2.34	-8.75	-0.55	-0.08

Table 4. Spatial and seasonal variations of key water parameters along flow pathway (w=winter samples, s=summer samples).

5. Discussion

5.1. Fluid types and origins

The high hydrochemical variety in nearby springs in earlier studies was related to interaction and mixing processes between thermal and surface waters (e.g. Tóth and Almási, 2001). This can be determined using the concentrations of major ions and the $\delta^{18}O$ and δD values to trace the mixing nature as well as the origin of the deep-seated water (e.g., Lee et al., 2011; Wang et al., 2013; Pérez-Zárate et al., 2015; Chatterjee et al., 2016, Yang et al., 2017). The Cl-HCO_3-SO_4 ternary diagram of Fig. 4a (Giggenbach,1988) allows to distinguish the Spring I waters, which fall in the mature (deep) Na-Cl field, with respect to those belonging to Spring II and Spring III, that mostly relate to the peripheral Ca(Na)-HCO_3 field. The Na-K-Mg ternary diagram (Giggenbach,1988) advocates partially equilibrated

waters for Spring I and immature waters for Spring II and III (Fig. 4B). Moreover, stable isotope signatures of waters have widely been applied to define the origin of thermal waters and trace fluid circulation and fluid-rock interactions (e.g. Craig, 1961; Clark and Fritz, 1997; Pastorelli et al., 1999; Chandrajith et al., 2013; Chatterjee et al., 2016). The $\delta^{18}O$ versus δD values of the NW Gorveh waters are plotted in Fig. 5 and compared with the Global Meteoric Water Line (GMWL; Craig, 1961) as well as the Mediterranean Meteoric Water Line (MMWL; IAEA, 1981). In general, the samples plot relatively close to the GMWL, pointing to meteoric origin of the waters sampled, which is consistent with other studies documenting a meteoric origin for thermal waters worldwide (e.g. Grasby et al., 2000; Ahmad et al., 2001; Lee et al., 2011; Moreira and Fernández, 2015; Yang et al., 2017). However, the distribution of $\delta^{18}O$ (V-SMOW) and δD (V-SMOW) of ongoing springs point toward different recharge sources corresponding to different active sub-watershed regions.

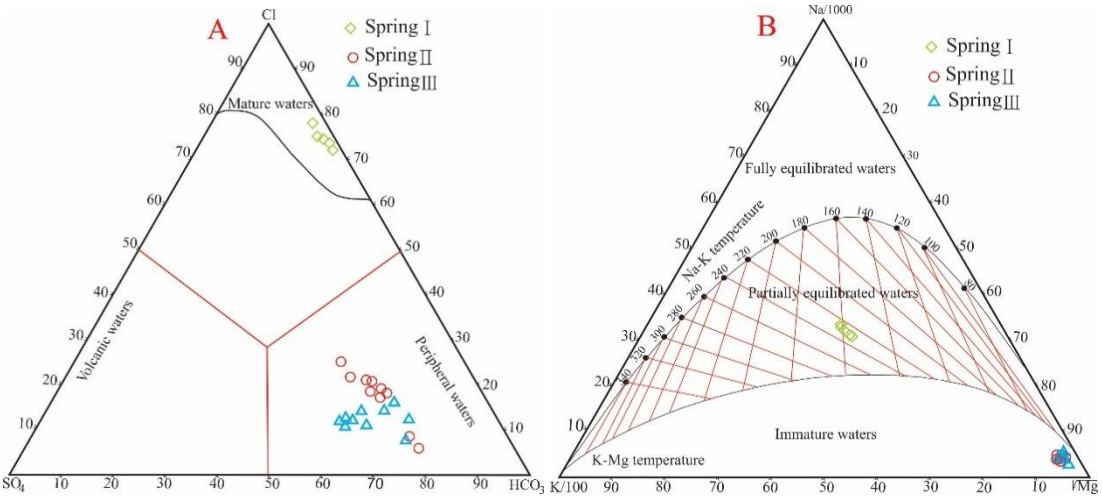


Fig. 4. A) Cl - SO_4 - HCO_3 triangular diagram for the waters listed in Table 1 and used to classify geothermal waters (based on Giggenbach,1988). B). Distribution of the water samples from Spring I, Spring II and Spring III listed in Table 1 in the Na – K – Mg triangular diagram (Giggenbach, 1988).

The Spring I waters are a shifted to the right of the GMWL line (Fig. 5), possibly reflecting an oxygen isotope exchange with host rock at a temperature >150 °C (Gianelli and Teklemariam, 1993). Considering the regional geology, this meteoric water therefore was likely affected by long term fluid-rock interaction with host rocks. Fluid-rock interaction between meteoric water and the host rocks

explains the very high Na^+ and Cl^- contents (as further argued below) together with moderate Ca^{2+} in Spring I type waters.

The Spring II waters are very well grouped and no significant variations are recorded in terms of time and space. Nevertheless, the stable isotopic data are distinctly different from those of Spring I. This is possibly reflecting either a different discharge and/or different fluid circuit with shorter residence time. Regarding to its meteoric origin based on Fig. 5, the fractionation in $\delta^{18}O$ and δD in hydrothermal waters compared to local water can be explained by water-rock interaction during water circulation in the subsurface and/or different age of source meteoric water. The water-rock interaction would have cause the higher TDS of Spring II rather than local water.

The distribution of the Spring III samples along the GMWL line clearly supports a different local discharge of the thermal fluids. This distribution in Spring III is especially observed in terms of time (Fig. 6) when the isotopic data are plotted versus TDS. The data indicate the mixing of two meteoric waters with almost the same TDS but with a different stable isotopic composition. The first meteoric water end member (station 4 in Spring III) is comparable to the composition ($\delta^{18}O$ and δD) of Spring II. This meteoric end member is not influenced by the seasonality similar to Spring I (Fig. 9). Therefore, most likely it has a deeper origin and a more constant flow. The low isotopic values compared to the current meteoric water values suggests that the origin of the meteoric water is different, i.e. in time or space. The second meteoric end member of the Spring III fluids especially becomes important during winter. However, it is not a classical fresh meteoric surface water since its TDS is comparable to Spring II fluid. Also this meteoric water interacted with rocks increasing its TDS. The response to the seasonality suggests this water has a shallower origin compared to the Spring II fluid end-member. The similarity of the stable isotopic composition compared to that of the current day meteoric water present in the area indicates this end –member Spring III fluid is very similar to the meteoric water present today in the immediate vicinity. For example, the present day meteoric water from snow, showing -6‰ for $\delta^{18}O$ (V-SMOW) and -27‰ for δD (V-SMOW) (Table 4) and local fresh water springs display $\delta^{18}O$ and δD (V-SMOW) values of -8‰ and between -48 to -53‰, respectively. It should be noted that the

end-member fluid did migrate in the deeper surface explaining its high TDS compared to the fresh meteoric water of the snow and water extraction sites. However, concerning the samples from summer and the main isolated discharge point of spring III in station 4 indicate a close relationship with Spring II.

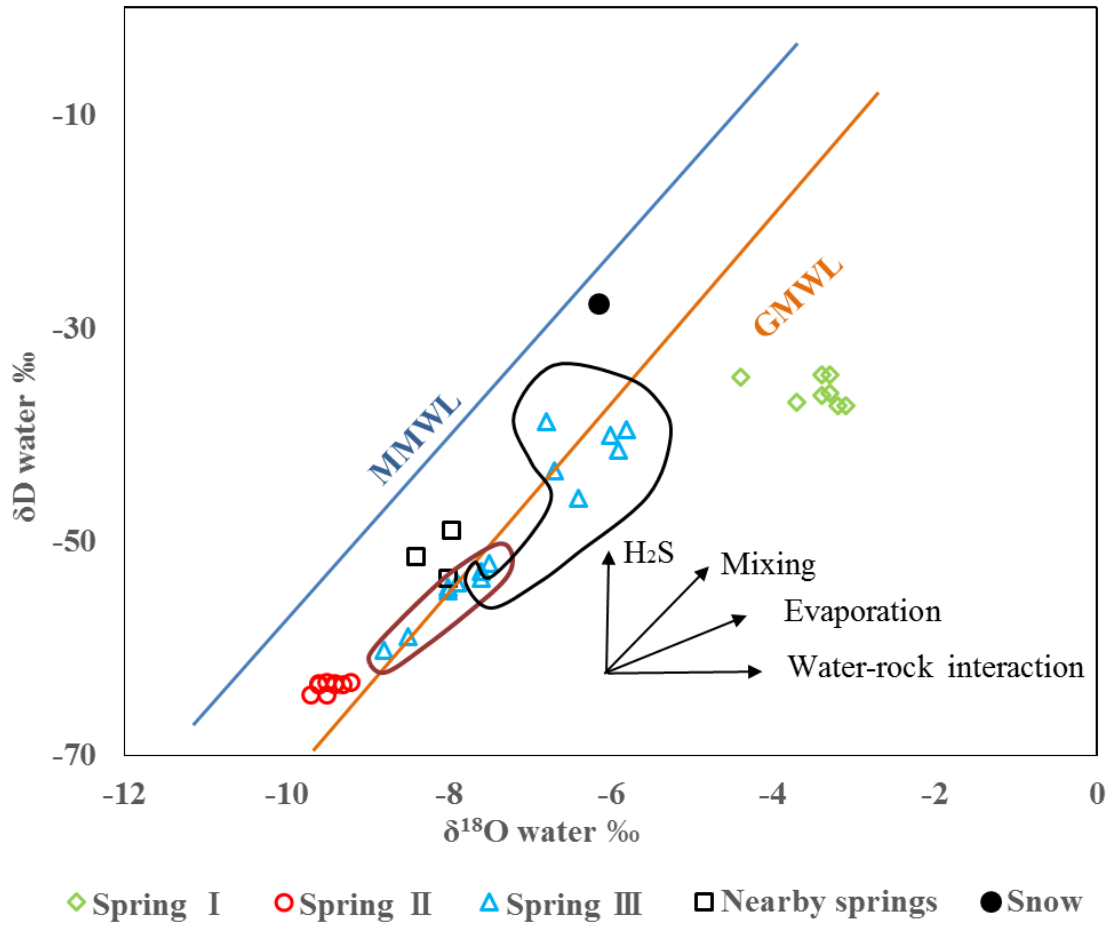


Fig. 5. Plot of $\delta^{18}O$-δD (V-SMOW) for the studied water samples. GMWL corresponds to the Global Meteoric Water Line (Craig, 1961) and MMWL represents the Mediterranean Meteoric Water Line (EMMWL; IAEA, 1981). Waters from Spring III can be divided into two groups: the dotted black field groups the winter (W) samples while the dotted red field includes the water samples collected in summer (S).

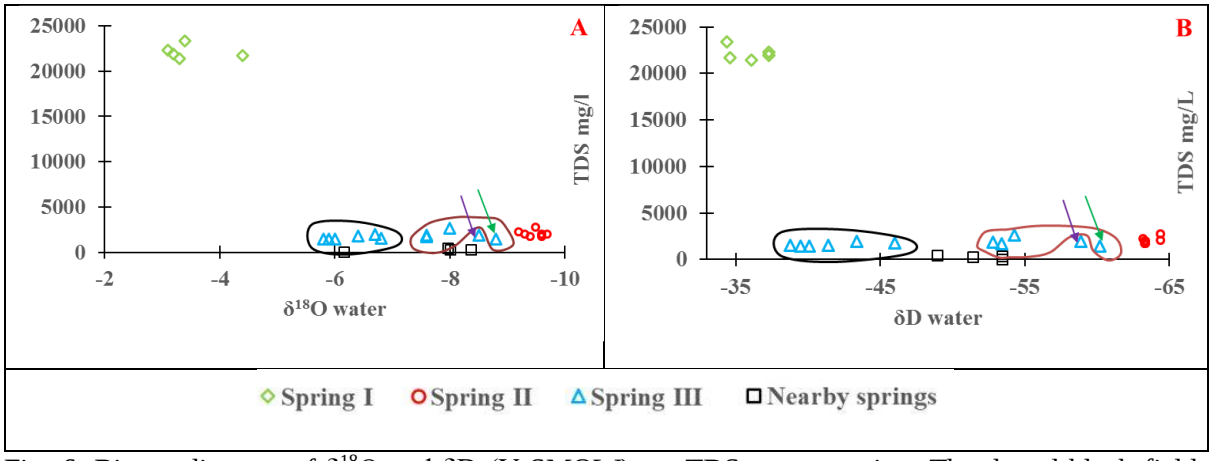


Fig. 6. Binary diagram of $\delta^{18}O$ and δD (V-SMOW) vs. TDS concentration. The dotted black fields include water samples collected from Spring III in winter while the dotted red fields are referred to those samples of Spring III collected in summer. The purple and green arrows are the samples from station 4 (Spring III) in winter and summer, respectively.

5.2. Controls on the major ion chemistry of studied thermal springs

Previous sedimentological, diagenetic and rock geochemical investigations in the study area (Mohammadi et al., 2019) argued that the geological substrate controls the difference in architecture, rock texture and fluid/rock interactions these deposits. Here, hydrochemistry properties of potentially related active springs are considered to provide insights into the source of major ions, since these presently active springs are responsible of local travertine precipitation. Spring I occurs adjacent to the fissure ridge and Springs II and III discharges next to the travertine mound. In general, underground waters are classified as oceanic, meteoric and evolved waters (Deming, 2002). Thermal water is considered as evolved water which originated from the ocean or atmosphere whose initial composition has been changed by physico-chemical processes (Goldscheider et al., 2010). As shown in Table 1 and Fig. 3, Spring I waters are dominated by Na^+ and Cl^-. The SI values of halite, gypsum and anhydrite (Table 3) suggest undersaturation conditions for these evaporitic minerals. The stoichiometry between Cl^- and Na^+ would suggest that these solutes are sourced by either dissolution of halite according to a steady state dissolution process or a fluid of geothermal origin (Grasby et al., 2000). The second predominant anion is HCO_3^- whose concentration is much higher than that of Ca^{2+}. Consequently, HCO_3^- is likely associated with the presence of a CO_2-rich gas phase that partially solubilizes into the

water. SO_4^{2-} in hydrothermal fluids originates according to Grasby et al. (2000), from either gypsum and/or anhydrite or the oxidation of pyrite. The positive correlation between Ca^{2+} and SO_4^{2-} suggests that gypsum/anhydrite likely contributed to the presence of sulfate in solution, although additional sources for Ca^{2+} (and Mg^{2+}) are to be regarded as derived by dissolution of carbonate rocks. It should be noted that addition of Ca^{2+} from the dissolution of gypsum or/and anhydrite causes a solubility reduction of $CaCO_3$ and $CaMg(CO_3)_2$ (e.g. Plummer et al., 1990; Bischoff et al., 1994; Dobrzyński, 2007; Jin et al., 2010). Yang et al. (2017, 2019) described this phenomenon as the common ion effect, which would explain why the SI of aragonite, calcite and dolomite are positive (Table 3).

The Spring I waters also contain marked enrichments in trace elements such as Li, B, Rb and Sr when compared to the concentrations of the same solutes from Spring II and Spring III. In general, high concentration of trace element in hydrothermal waters result from host rock leaching and basically, longer residence time favors water-rock interaction processes, which result in an increase in terms of contents of the trace elements (Ma et al., 2011). Therefore, fluid-mobility and varying degrees of conservative behavior of some trace elements (e.g. Li, B and Cl) have been employed to trace fluid source components (e.g., Seyfried et al., 1984; Ryan and Langmuir, 1987; Peacock and Hervig, 1999; Scambelluri et al., 2004). The presence of Li, B and Rb, likely relates to deep water circulation subject to high temperatures (Giggenbach, 1992). Leaching and ion exchange of Li, B and Rb are in relation to fluid-rock reaction with dominant protoliths (e.g. rhyolite, andesite and greywacke) (Reyes and Trompetter, 2012). It is worth to mention that both andesites and metamorphic rocks are widely present in the substrate of the study area. Rb is considered as a mobile element in hydrothermal settings and behaves like K. Consequently, its concentration is intimately related to that of K, which is also relatively high due to the presence of andesitic rocks in the subsurface. High Sr contents can also be attributed to andesites or exchange with carbonates containing high Sr contents. The Qom Formation is a likely candidate reservoir as proposed by Mohammadi et al. (2019) as it consists of both calcite and evaporite as well as extended karstification which makes it a good reservoir. This formation is also regarded as one of the main important petroleum reservoirs in central Iran (Reuter et al., 2009).

As reported in Tables 2 and 3, the concentration of the main solutes and trace elements (e.g. B and Li) in Spring I is much higher than that determined for the waters discharging from Spring II and III. This can be explained by different fluid-rock interactions and (as argued below) likely shorter hydrological circuits, which is in agreement with the peripheral nature of these fluids as inferred from the Cl-HCO_3-SO_4 ternary diagram (Fig. 4a). According to the local geological setting, and aforementioned acquired data a mixture of both carbonate and volcanic (tuffs, lapilli, tuffs and pumiceous tuffs) rock types likely acted as the main reservoir for these waters.

5.3. Origin of dissolved Carbon in the fluid

The DIC derived directly from the dissolution of carbonate rocks can be calculated, as follows: $C_{carb} = (Ca + Mg) - SO_4$ (Chiodini et al., 2004) whereas the presence of a distinct (deep) source of carbon is based on the following formula $C_{ext} = DIC - C_{carb}$. The origin of C_{ext} can be estimated based on following equation of $\delta^{13}C_{DIC} \times DIC = \delta^{13}C_{ext} \times C_{ext} + \delta^{13}C_{carb} \times C_{carb}$. In our case, since the carbonate reservoir likely corresponds to the Qom Formation with $\delta^{13}C$ values varying between -0.84 and +1.47‰ (Ballato et al., 2011), the average range of $\delta^{13}C_{ext}$ for Springs I, II and III varies between +3.9 to +9.2‰, -0.4 to +1.4‰ and -0.6 to +0.5‰, respectively. Plotting these values in Fig. 7 shows that the values for the three springs plotted above -2‰ with high DIC values indicating carbon originating from a deep, mantle-related source.

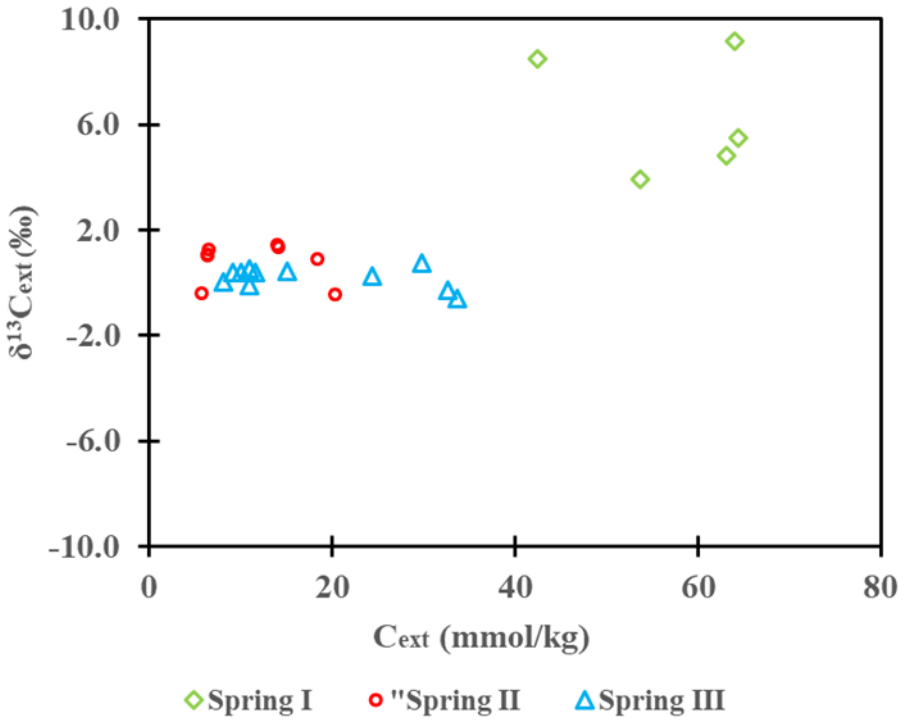


Fig. 7. Graph of $\delta\,^{13}C_{ext}$ versus $C_{ext.}$ (The "ext" index is the carbon that originates from other sources apart from carbonate mineral).

5.4. Reservoir type, temperature and depth

According to Souther (1992), springs can be divided into 3 groups based on their geological association: i.e. (1) carbonate-hosted springs, (2) silicate-hosted springs (igneous and metamorphic rock in non-volcanic regions) and (3) springs hosted in Quaternary volcanic belts. Regarding the main characteristics of carbonate-hosted springs they are characterized by high TDS and low SiO_2. According to the relatively high TDS and low SiO_2 values from Spring I (Table 1), these waters have concentrations similar to those reported for carbonate-hosted springs by Grasby et al., (2000). Thus, the reservoir of Spring I waters can be considered as of carbonate type. As far as Spring II and III are concerned, the TDS values are lower and the SiO_2 concentrations are slightly higher than those from Spring I, which can be associated with a Quaternary volcanic belts origin. Moreover, the presence of dry gas discharge with smell of rotten eggs pointing to hydrogen sulfide together with active/semi-active volcanism nearby this area reported by Azizi et al. (2013) potentially pointing to interactions with the Quaternary volcanic belts.

Several cation geothermometers have been applied to water from wells in geothermal areas to estimate equilibrium reservoir temperatures. In this work, liquid and carbon isotope geothermometers were applied to the studied spring waters. While fluid-rock interaction and changes in geochemical conditions during upward migration might cause strong changes in fluid chemistry, some conservative cations or their ratios are possibly still of potential interest. Based on the K – Na – Mg- data and applying the approach proposed by Giggenbach (1988) water–rock equilibrium and mixing processes can be assessed (see Fig. 4B). Plotting Spring I samples on this diagram their values occur in the area of pertaining to partially equilibrated water. Moreover, the reservoir temperatures can be calculated based on the Na-Li geothermometer which was proposed by Fouillac and Michard (1981): $T_{Na-Li} = 1049/[\lg (Na/Li) + 0.44] – 273.15$ and the Na–K geothermometer suggested by Giggenbach (1988): $T_{Na-K} = 1390/[1.75 – \lg (Na/K)] – 273.15$. By applying these two geothermometers on Spring I waters, temperatures of 230 °C and 190 °C were computed. Since the exchange of B and Li in fluid-rock interaction systems is also temperature-dependent, the equilibrium temperature at which fluid-rock interaction took place based on these variables can also be estimated. When the temperature is <180 °C, boron (B) mobility decreases due to its uptake by clay minerals (Reyes and Trompetter, 2012). Fluid mobility of lithium (Li) also decreases substantially at >200 °C ± 20 °C (Reyes and Trompetter, 2012). The Li and B content presented above supports such a high temperature in Spring I. Furthermore, fluid carbon isotope signatures show values varying around 3.7 ‰ that are close to the proposed source carbonate signature (with an average of 1.3 ‰) related to the Qom Formation. This suggests absence or even a positive carbon isotope fractionation, indicating temperatures ≥ 200 °C (Friedman and O'Neil, 1977). Consequently, all these parameters point towards initial temperatures higher than 190 °C for Spring I.

Spring II and III samples plot in the field of immature water (see Fig. 4B), suggesting short residence time and probably different fluid circulation. Application of the Na-Li (Fouillac and Michard, 1981) geothermometer gave equilibrium temperatures for Spring II and III of 110 °C and 90 °C, respectively. The study area is known for its geothermal potential (Yousefi et al., 2010), being part of the Hmadean – Tabriz volcanic belt with active volcanism located nearby. According to Afshar et al. (2017) and

Ebrahimi et al. (2019) for the Tabriz area around the Sabalan volcanic center, a geothermal gradient between 40 to 60 °C per kilometer was computed. The reservoir depth was calculated based on Cheng et al. (2015) formula of $Z = T_z - T_0/G$. Here Z is the circulation depth in m, T_z is calculated reservoir temperature (°C) from geothermometry and G is thermal gradient of the area (°C/m). If the computed equilibrium temperatures are considered as realistic, the depth of the reservoirs is ~ 3-4 km for Spring I waters and 1-2 km for Spring II and III waters.

5.5. Conceptual model

Based on above results and discussion a conceptual model of the distinct hydrological circuits for Spring I, II and III is reported in Fig. 8. The three fluids originated from meteoric water. Fluid I that dominates Spring I activity originates from a deep carbonate aquifer and likely experienced long residence time. The fluid II that dominates Spring II and partialy Spring III waters, circulated among both carbonate and volcanic rock in shallower depth. Fluid III that mainly interfered in winter in Spring III experienced circulation in shallower depth than Spring II as the isotope values are close to analysed fresh water signatures of surrounding springs. This interpretation also supports the hypothesis proposed by Mohammadi et al. (2019) that different substrate controls different aspects of travertine characteristics and consequently water chemistry. This means that, based on integration of hydrochemical and geological data it is possible to deduce the hydrothermal reservoir, its depth and temperature in addition to information on fluid flow path, fluid mixing and fluid-rock interaction. It should be noted that the differences between the conceptual models of the hydrogeology and travertine deposits (Mohammandi et al., 2019, fig. 13) is related to their difference in time. Despite obvious similarities in the location of the massive travertine deposits and the active travertine spring precipitates (Spring I, next to the sparite-dominated fissure ridge is still precipitating sparite, and Spring Ⅱ and Ⅲ are precipitating micrite), some distinct differences are present. Two important parameters have changed, namely the volume and the temperature of the water. A higher fluid discharge rate in the past can be assumed based on the vast extension of fossil geobodies in this area that cannot be explained by present-day discharge rates. The higher temperature in the past was calculated based on the formula given by Kele et al. (2011). This change in temperature can be related to tectonic inactivity and volcanism, a decrease in water volume

resources and/or a change in depth of circulation. After considering the several scenario´s, the most likely model was drawn.

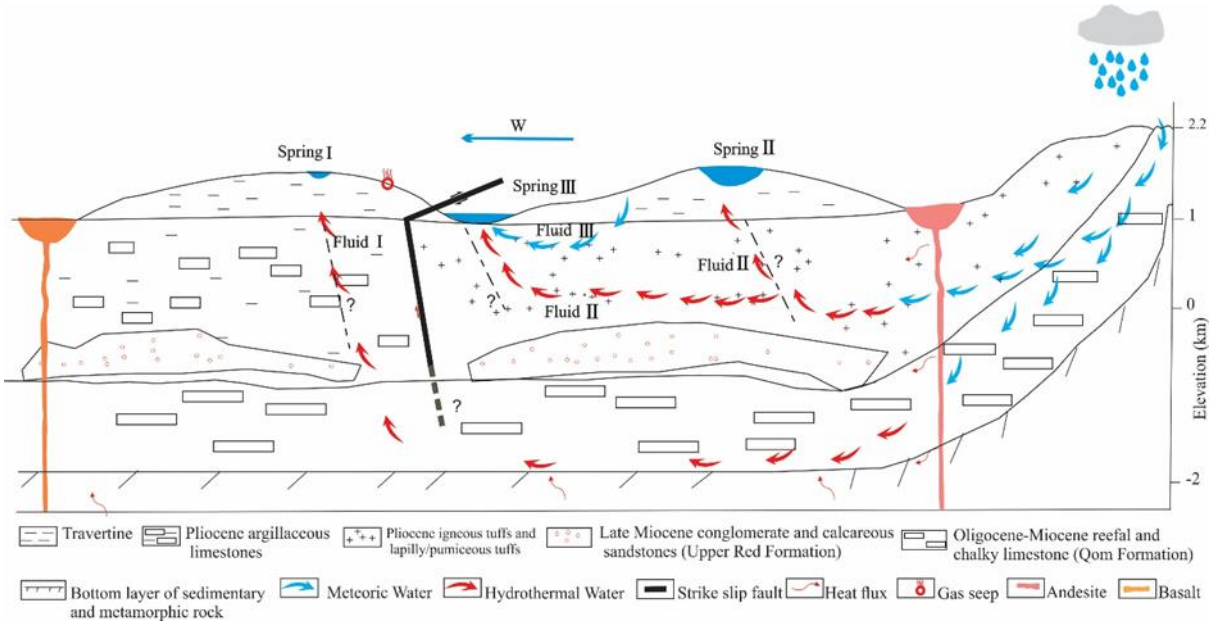


Fig. 8. Conceptual regional flow model of different fluid circuits (not to scale).

5.6. Spatial and seasonal variations

The strong positive correlation between alkalinity, pCO_2, pH, Ca^{2+} and DIC concentration from the orifice to downstream for each sampling site indicates a common controlling process active in the travertine precipitating water (Fig. 9). This can be explained by CO_2 evasion, which causes an increase in water pH (e.g. Johnson et al., 2008) and substantially facilitates the precipitation of $CaCO_3$. Consequently, a portion of the alkalinity (HCO_3^-), DIC and Ca^{2+} from the water is consumed. Therefore, going away from the orifice the concentration of these components tends to decrease. Moreover, fast and turbulent flow and the confluence along the main paths of high-altitude tributaries further increase the CO_2 evasion and the pH favoring the precipitation of travertine (Kele et al., 2011). A strong inverse correlation between pCO_2 and $\delta^{13}C_{DIC}$ signature, which rapidly becomes enriched downstream, evidences the rapid degassing downstream (Fig. 9), which produces increasingly positive isotopic values of $\delta^{13}C_{DIC}$ (e.g. Gonfiantini et al., 1968; Chafetz and Lawrence 1994; Tamooh et al., 2013).

Such a systematic decrease of pCO_2 without any correlation with the low concentrations of POC and DOC points towards a homogeneous carbon source. This means that the main or even the only source of carbon is likely residing in the thermal system. The $\delta^{18}O$ and δD values showed no significant variation along their pathway, which can be related to minor to no evaporation due to normal ambient surface water temperatures.

In terms of temporal variation, samples from orifice of Spring I, II and end member of Spring III (station 4 in Spring III) display decrease in HCO_3^- and pCO_2 content during the winter, while the other parameters (e.g. TDS, $\delta^{18}O$ and δD) remain almost the same as during summer (Fig. 9). Above discussion indicated that huge amount of HCO_3^- originated from CO_2,. Therefore, the possible explanation can be either different degassing due to changing in the season and accordingly temperature or different CO_2 source. However, $\delta^{13}C_{DIC}$ should be influenced as well, if any of aforementioned reasons caused difference in CO_2 concentration in springs. As $\delta^{13}C_{DIC}$ remains almost the same during both seasons for each spring vent, a possible reason can point to a same source for CO_2 but with different volume of CO_2 input. However, for further explanation the measurement from several seasons are necessary which is out of scope of this study.

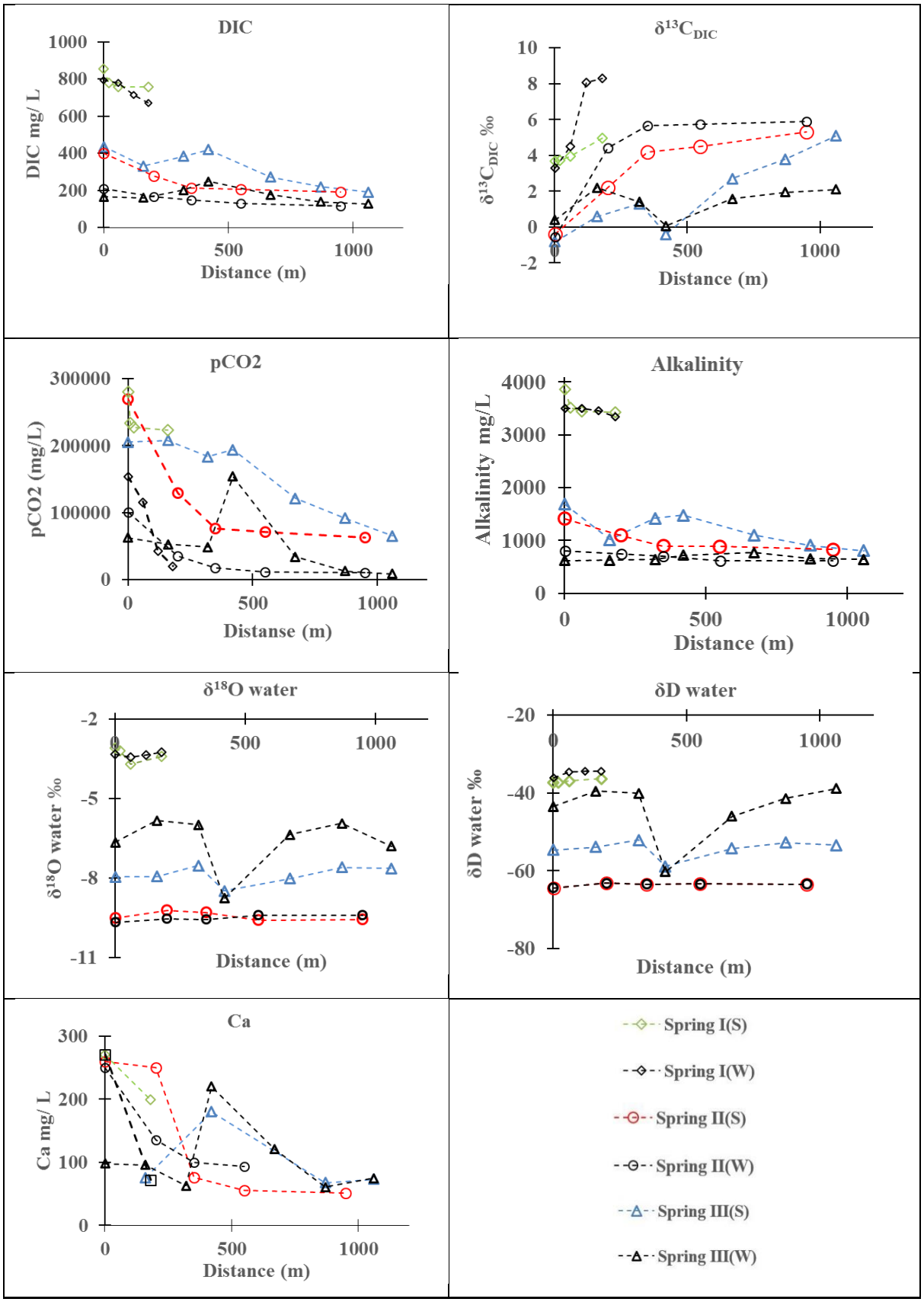


Fig. 9. Graphs of some of the key water geochemistry parameters in summer and winter.

6. Conclusions

The conclusions can be summarized in the following bullet points:

- The travertine water from the Babagorgor watershed points to a deep origin >1-2 km of both carbonate and volcanic reservoir type.
- The Qom Formation (Oligo-Miocene) represents the most plausible main carbonate reservoir. Na^+ and Cl^- originate from the dissolution of halite in the strata. The positive covariation between Ca^{2+} and SO_4^{2-} points to dissolution of gypsum and anhydrite interlayers. Dissolution of carbonate is restrained by the common ion effect, resulting from evaporite dissolution. The relatively low value of Ca^{2+} in comparison with HCO_3^- results from additional dissolution of CO_2.
- The springs from Babagorgor represent different hydrofacies: mature (deep) waters of the chloride type Na-Cl (Spring I) and more peripheral (superficial) waters of the dilute chloride-bicarbonate type (mixed with Ca-Na-HCO_3; Springs II and III)
- Based on cation and stable carbon isotope thermometry the average reservoir temperatures are ~210, 110 and 90 °C for Spring I, II and III, respectively.
- The hydrochemistry, geothermometry and the local geology show that the fluid circulated at a depth of 3-4 km for Spring I and 1-2 km for Spring II and III.
- Based on the hydrochemical variation of the spring waters along their flow paths, there is significant CO_2 degassing and limited to no evaporation.
- During the winter season, apart from decreasing CO_2 content that probably is due to lower volume input, the chemical composition does not show any clear difference at their orifice compared with summer. This suggest low temporal variation which best can be explained by the existence of deep sourced.
- In the three investigated sites, inorganic travertine precipitation strongly dominates.

7. Acknowledgements

The authors are grateful to Prof. Dr. Ir. S. Bouillon and colleagues of the Department of Earth and Environmental Sciences of the KU Leuven (Belgium) for performing the DIC, DOC, POC, PIC concentration and oxygen, hydrogen and carbon stable isotope measurements. Prof. Dr. A. Borges (Chemical Oceanography department (AGO-FOCUS), Liège University) is gratefully appreciated for performing the pCO_2 concentration. Mr. K. Amjadian and Mr. H. Abbasi are thanked for their help during fieldwork. Dr. E. Vassilieva is acknowledged for the ICP-OES analysis. This work was supported by KU Leuven research and development.

8. References

Acikel, S. and Ekmekci, M., 2016. Hydrochemical characterization of Pamukkale travertines, Denizli, Turkey, for remediative measures. Environmental Earth Sciences, 75(22), 1456.

Afshar, A., Norouzi, G.H., Moradzadeh, A., Riahi, M.A. and Porkhial, S., 2017. Curie Point Depth, Geothermal Gradient and Heat-Flow Estimation and Geothermal Anomaly Exploration from Integrated Analysis of Aeromagnetic and Gravity Data on the Sabalan Area, NW Iran. Pure and Applied Geophysics, 174(3), 1133–1152.

Ahmad, M., Akram, W., Hussain, S. D., Sajjad, M. I., and Zafar, M. S., 2001. Origin and subsurface history of geothermal water of Murtazabad area, Pakistan–isotopic evidence. Applied Radiation and Isotopes, 55(5), 731–736.

Alavi, M., 2004. Regional stratigraphy of the Zagros fold-thrust belt of Iran and its proforeland evolution. American Journal of Science, 304(1), 1–20.

Alçiçek, H., Bülbül, A., Yavuzer, İ. and Alçiçek, M.C., 2019. Origin and evolution of the thermal waters from the Pamukkale Geothermal Field (Denizli Basin, SW Anatolia, Turkey): Insights from hydrogeochemistry and geothermometry. Journal of Volcanology and Geothermal Research, 372, 48–70.

Allen, M.B., Saville, C., Blanc, E.P., Talebian, M. and Nissen, E., 2013. Orogenic plateau growth: Expansion of the Turkish-Iranian Plateau across the Zagros fold-and-thrust belt. Tectonics, 32(2), 171–

190.

Azizi, H., Asahara, Y., Tsuboi, M., 2013. Quaternary high-Nb basalt: existence of young oceanic crust under the Sanadaj-Sirjan zone, NW Iran. International Geology Review, 56, 167–186.

Ballato, P., Uba, C.E., Landgraf, A., Strecker, M.R., Sudo, M., Stockli, D.F., Friedrich, A. and Tabatabaei, S.H., 2011. Arabia-Eurasia continental collision: Insights from late Tertiary foreland-basin evolution in the Alborz Mountains, northern Iran. Bulletin, 123(1-2), 106–131.

Bischoff, J.L., Juliá, R., Shanks III, W.C. and Rosenbauer, R.J., 1994. Karstification without carbonic acid: Bedrock dissolution by gypsum-driven dedolomitization. Geology, 22(11), 995–998.

Brogi, A., Alçiçek, M.C., Yalçıner, C.Ç., Capezzuoli, E., Liotta, D., Meccheri, M., Rimondi, V., Ruggieri, G., Gandin, A., Boschi, C. and Büyüksaraç, A., 2016. Hydrothermal fluids circulation and travertine deposition in an active tectonic setting: insights from the Kamara geothermal area (western Anatolia, Turkey). Tectonophysics, 680, 211–232.

Brogi, A., Capezzuoli, E., Kele, S., Baykara, M.O. and Shen, C.C., 2017. Key travertine tectofacies for neotectonics and palaeoseismicity reconstruction: effects of hydrothermal overpressured fluid injection. Journal of the Geological Society, 174(4), 679–699.

Boccaletti, M., Innocenti, F., Manetti, P., Mazzuoli, R., Motamed, A., Pasquare, G., di Brozolo, F.R. and Sobhani, E.A., 1976. Neogene and Quaternary volcanism of the Bijar area (western Iran). Bulletin Volcanologique, 40(2), 121–132.

Capezzuoli, E., Gandin. A. and Pedley. H.M. 2009. Travertines and calcareous tufa in Tuscany (Central Italy). In: Sedimentary of Mediterranean Islands. Field Trip Guide Book 27th IAS Meeting (Eds. V. Pascucci and S. Andreucci). Field trip 7. 129–158.

Chafetz, H. and Lawrence, J., 1994. Stable isotopic variability within modern travertines. Géographie physique et Quaternaire, 48(3), 257–273.

Chandrajith, R., Barth, J.A., Subasinghe, N.D., Merten, D. and Dissanayake, C.B., 2013. Geochemical

and isotope characterization of geothermal spring waters in Sri Lanka: evidence for steeper than expected geothermal gradients. Journal of Hydrology, 476, 360–369.

Chatterjee, S., Sharma, S., Ansari, M.A., Deodhar, A.S., Low, U., Sinha, U.K. and Dash, A., 2016. Characterization of subsurface processes estimation of reservoir temperature in Tural Rajwadi geothermal fields, Maharashtra, India. Geothermics, 59, 77–89.Cheng, Q., Yang, H., Zeng, M., 2015. The formation and protection of karst geothermal water resources in the main urban area of Chongqing. Carsologica Sin, 34 (3), 217–227.

Chiodini, G., Cardellini, C., Amato, A., Boschi, E., Caliro, S., Frondini, F. and Ventura, G., 2004. Carbon dioxide Earth degassing and seismogenesis in central and southern Italy. Geophysical Research Letters, 31(7).

Claes, H., Huysmans, M., Soete, J., Dirix, K., Vassilieva, E., Marques Erthal, M., Vandewijngaerde, W., Hamaekers, H., Aratman, C., Özkul, M., Swennen, R., 2019. Elemental geochemistry to complement stable isotope data of fossil travertine: Importance of digestion method and statistics. Sedimentary Geology 386, 118–131.

Clark, I.D., Fritz, P., 1997. Environmental Isotopes in Hydrogeology. Lewis Publishers, New York.

Craig, H., 1961. Isotopic variation in meteoric waters. Science 133, 1702–1703.

Deming, D., 2002. Introduction to hydrogeology. McGraw-Hill College, New York, 468 pp.

Dobrzyński, D., 2007. Chemical diversity of groundwater in the Carboniferous–Permian aquifer in the Unisław Śląski–Sokołowsko area (the Sudetes, Poland); a geochemical modelling approach. Acta Geologica Polonica, 57(1), 97–112.

Ebrahimi, D., Nouraliee, J. and Dashti, A., 2019. Inspecting geothermal prospects in an integrated approach within the West Azarbaijan Province of Iran. Geothermics, 77, 224–235.

Friedman, I. and O'Neil, J.R., 1977. Data of Geochemistry: Compilation of Stable Isotope Fractionation Factors of Geochemical Interest. United States Department of the Interior, Geological Survey.

Ford. T.D. and Pedley. H.M. 1996. A review of tufa and travertine deposits of the World. Earth Science Review. 41. 117–175.

Fouillac, C. and Michard, G., 1981. Sodium/lithium ratio in water applied to geothermometry of geothermal reservoirs. Geothermics, 10(1), 55–70.

Fouke, B.W., Farmer, J.D., Des Marais, D.J., Pratt, L., Sturchio, N.C., Burns, P.C. and Discipulo, M.K., 2000. Depositional facies and aqueous-solid geochemistry of travertine-depositing hot springs (Angel Terrace, Mammoth Hot Springs, Yellowstone National Park, USA). Journal of Sedimentary Research, 70(3), 565–585.

Fouke, B.W., 2011. Hot-spring systems geobiology: abiotic and biotic influences on travertine formation at Mammoth Hot Springs, Yellowstone National Park, USA. Sedimentology, 58(1), 170–219.

Gat, J.R. and Carmi, I., 1970. Evolution in the isotopic composition of atmospheric waters in the Mediterranean Sea area. Journal of Geophysical Research, 75, 3039–3048.

Gianelli, G. and Teklemariam, M., 1993. Water-rock interaction processes in the Aluto-Langano geothermal field (Ethiopia). Journal of volcanology and geothermal research, 56(4), 429–445.

Giggenbach, W.F., 1988. Geothermal solute equilibria. derivation of Na-K-Mg-Ca geoindicators. Geochimica et Cosmochimica Acta, 52(12), 2749–2765.

Giggenbach, W.F., 1992. Isotopic shifts in waters from geothermal and volcanic systems along convergent plate boundaries and their origin. Earth and planetary science letters, 113(4495–510.

Giggenbach. W. F. and Glover. R. B., 1992. Tectonic regime and major processes governing the chemistry of water and gas discharges from the Rotorua geothermal field. New Zealand. Geothermics 21, 121–140.

Gillikin, D.P. and Bouillon, S., 2007. Determination of $\delta^{18}O$ of water and $\delta^{13}C$ of dissolved inorganic

carbon using a simple modification of an elemental analyser-isotope ratio mass spectrometer: an evaluation. Rapid Communications in Mass Spectrometry: An International Journal Devoted to the Rapid Dissemination of Up-to-the-Minute Research in Mass Spectrometry, 21(8), 1475–1478.

Gran, G., 1952. Determination of the equivalence point in potentiometric titrations. Part II. Analyst, 77(920), 661–671.

Grasby, S.E., Hutcheon, I. and Krouse, H.R., 2000. The influence of water–rock interaction on the chemistry of thermal springs in western Canada. Applied Geochemistry, 15(4), 439–454.

Grasby. S.E., van Everdingen. R.O., Bednarski. J. and Lepitzki. A.W., 2003. Travertine mounds of the Cave and Basin National Historic Site. Banff National Park. Can. J. Earth Sci.. 40. 1501–1513.

Goldscheider, N., Pronk, M. and Zopfi, J., 2010. New insights into the transport of sediments and microorganisms in karst groundwater by continuous monitoring of particle-size distribution. Geologia Croatica, 63(2),137–142.

Gonfiantini, R., Panichi, C. and Tongiorgi, E., 1968. Isotopic disequilibrium in travertine deposition. Earth and Planetary Science Letters, 5(1), 55–58.

GSI, 1999. Geology maps of Ghorveh and Kabudar Ahang regions, Western Iran, a Digitized final map at 1:100,000 Scale. Geological Survey of Iran, Tehan, Iran.

I.A.E.A, 1981. Stable isotope hydrology. Deuterium and oxygen-18 in water cycle. In: Gat,J.R., Gonfiantini, R. (Eds.), International Atomic Energy Agency Technical Report No. 210, Vienna (pp. 339).

Jin, L., Siegel, D.I., Lautz, L.K., Mitchell, M.J., Dahms, D.E. and Mayer, B., 2010. Calcite precipitation driven by the common ion effect during groundwater–surface-water mixing: A potentially common process in streams with geologic settings containing gypsum. GSA Bulletin, 122(7-8), 1027–1038.

Johnson, M.S., Lehmann, J., Riha, S.J., Krusche, A.V., Richey, J.E., Ometto, J.P.H. and Couto, E.G., 2008. CO2 efflux from Amazonian headwater streams represents a significant fate for deep soil respiration. Geophysical Research Letters, 35(17).

Jones, B. and Renaut, R.W., 2010. Calcareous spring deposits in continental settings. Developments in Sedimentology, 61, 177–224.

Karimi Nezhad, M.T., Mohammadi, K., Gholami, A., Hani, A., Shariati, M.S., 2014. Cadmium and mercury in topsoils of Babagorogor watershed, western Iran: distribution, relationship with soil characteristics and multivariate analysis of contamination sources. Geoderma, 219, 177–185.

Kele, S., Özkul, M., Fórizs, I., Gökgöz, A., Baykara, M.O., Alçiçek, M.C. and Németh, T., 2011. Stable isotope geochemical study of Pamukkale travertines: new evidences of low-temperature non-equilibrium calcite-water fractionation. Sedimentary Geology, 238(1-2), 191–212.

Keppel, M.N., Clarke, J.D., Halihan, T., Love, A.J. and Werner, A.D., 2011. Mound springs in the arid Lake Eyre South region of South Australia: a new depositional tufa model and its controls. Sedimentary Geology, 240(3-4), 55–70.

Keppel, M.N., Post, V.E., Love, A.J., Clarke, J.D. and Werner, A.D., 2012. Influences on the carbonate hydrochemistry of mound spring environments, Lake Eyre South region, South Australia. Chemical Geology, 296, 50–65.

Keshavarzi, B., Moore, F., Mosaferi, M. and Rahmani, F., 2011. The source of natural arsenic contamination in groundwater, west of Iran. Water Quality, Exposure and Health, 3(3-4), 135–147.

Kratz, T.K., Schindler, J., Hope, D., Riera, J.L. and Bowser, C.J., 1997. Average annual carbon dioxide concentrations in eight neighboring lakes in northern Wisconsin, USA. Internationale Vereinigung für theoretische und angewandte Limnologie: Verhandlungen, 26(2), 335–338.

Lee, S.G., Kim, T.K. and Lee, T.J., 2011. Strontium isotope geochemistry and its geochemical

implication from hot spring waters in South Korea. Journal of Volcanology and Geothermal Research, 208(1-2), 12–22.

Linares, R., Rosell, J., Roqué, C. and Gutiérrez, F., 2009. Origin and evolution of tufa mounds related to artesian karstic springs in Isona area (Pyrenees, NE Spain). Geodinamica Acta, 22(5–6/1–3), 129.

Liu, Z., Zhang, M., Li, Q. and You, S., 2003. Hydrochemical and isotope characteristics of spring water and travertine in the Baishuitai area (SW China) and their meaning for paleoenvironmental reconstruction. Environmental Geology, 44(6), 698–704.

Liu, Z., Sun, H., Baoying, L., Xiangling, L., Wenbing, Y. and Cheng, Z., 2010. Wet-dry seasonal variations of hydrochemistry and carbonate precipitation rates in a travertine-depositing canal at Baishuitai, Yunnan, SW China: implications for the formation of biannual laminae in travertine and for climatic reconstruction. Chemical Geology, 273(3–4), 258–266.

Ma, R., Wang, Y., Sun, Z., Zheng, C., Ma, T., Prommer, H., 2011. Geochemical evolution of groundwater in carbonate aquifers in Taiyuan, northern China. Applied Geochemistry, 26, 884–897.

Mehrbach, C., Culberson, C.H., Hawley, J.E. and Pytkowicx, R.M., 1973. Measurement of the apparent dissociation constants of carbonic acid in seawater at atmospheric pressure 1. Limnology and Oceanography, 18(6), 897–907.Mohammadi, Z., Capezzuoli, E., Claes, H., Alipoor, R., Muchez, P. and Swennen, R., 2019. Substrate geology controlling different morphology, sedimentology, diagenesis and geochemistry of adjacent travertine bodies: a case study from the Sanandaj-Sirjan zone (western Iran). Sedimentary Geology, 389, 127–146.

Mohammadi, Z., Claes, H., Capezzuoli, E., Mozafari, M., Soete, J., Aratman, C. and Swennen, R., 2020. Lateral and vertical variations in sedimentology and geochemistry of sub-horizontal laminated

travertines (Çakmak quarry, Denizli Basin, Turkey), Quaternary International, 540, 146–168.

Moreira, P. and Fernández, R.R., 2015. La Josefina Au–Ag deposit (Patagonia, Argentina): a Jurassic epithermal deposit formed in a hot spring environment. Ore Geology Reviews, 67, 297–313.

Nicholson, K., 1993, Geothermal Fluids : Chemistry and Exploration Techniques, Springer-Verlag, UK.

Parkhurst, D.L. and Appelo, C.A.J., 1999. User's guide to PHREEQC (Version 2): A computer program for speciation, batch-reaction, one-dimensional transport, and inverse geochemical calculations. Water-resources investigations report, 99(4259), 312.

Pastorelli, S., Marini, L. and Hunziker, J.C., 1999. Water chemistry and isotope composition of the Acquarossa thermal system, Ticino, Switzerland. Geothermics, 28, 75–93.

Peacock, S.M. and Hervig, R.L., 1999. Boron isotopic composition of subduction-zone metamorphic rocks. Chemical Geology, 160(4), 281–290.

Pentecost, A., 2005. Travertine. Springer-Verlag, Berlin Heidelberg. 445 pp.

Pérez-Zárate, D., Santoyo, E., Guevara, M., Torres-Alvarado, I.S., Peiffer, L. and Martínez-Frías, J., 2015. Geochemometric modeling and geothermal experiments of Water/Rock Interaction for the study of alkali-feldspars dissolution. Applied Thermal Engineering, 75, 1244–1261.

Plummer, L.N., Busby, J.F., Lee, R.W. and Hanshaw, B.B., 1990. Geochemical modeling of the Madison aquifer in parts of Montana, Wyoming, and South Dakota. Water Resources Research, 26(9), 1981–2014.

Reuter, M., Piller, W.E., Harzhauser, M., Mandic, O., Berning, F., Kroh, A., Aubry, M.P., Wielandt-Schuster, U., Hamedani, A., 2009. The Oligo- Miocene Qom Formation (Iran): evidence for an early Burdigalian restriction of the Tethyan Seaway and closure of its Iranian gateways. Int. J. Earth Sci. 98, 627–650.

Reyes, A.G. and Trompetter, W.J., 2012. Hydrothermal water–rock interaction and the redistribution

of Li, B and Cl in the Taupo Volcanic Zone, New Zealand. Chemical Geology, 314, 96–112.

Ryan, J.G. and Langmuir, C.H., 1987. The systematics of lithium abundances in young volcanic rocks. Geochimica et Cosmochimica Acta, 51(6), 1727–1741.

Sahandi, M.R., Delavar, ST., Sadeghi, M., Jafari A. and Moosavi, A., 2005. Geological map of Iran (1:1,000,000) Geological Survey of Iran.

Scambelluri, M., Müntener, O., Ottolini, L., Pettke, T.T. and Vannucci, R., 2004. The fate of B, Cl and Li in the subducted oceanic mantle and in the antigorite breakdown fluids. Earth and Planetary Science Letters, 222(1), 217–234.

Seyfried Jr, W.E., Janecky, D.R. and Mottl, M.J., 1984. Alteration of the oceanic crust: implications for geochemical cycles of lithium and boron. Geochimica et Cosmochimica Acta, 48(3), 557–569.

Souther, J. G. 1992. Geothermal energy. Gabrielse, H., Yorath. CJ (Eds.), Geology of the Cordilleran Orogen in Canada, 787–792.

Tamooh, F., Borges, A.V., Meysman, F., Van den Meersche, K., Dehairs, F., Merckx, R. and Bouillon, S., 2013. Dynamics of dissolved inorganic carbon and aquatic metabolism in the Tana River basin, Kenya. Biogeosciences, 10, 6911–6928.

Teboul, P.A., Durlet, C., Gaucher, E.C., Virgone, A., Girard, J.P., Curie, J., Lopez, B. and Camoin, G.F., 2016. Origins of elements building travertine and tufa: New perspectives provided by isotopic and geochemical tracers. Sedimentary geology, 334, 97–114.

Teodoru, C.R., Del Giorgio, P.A., Prairie, Y.T. and Camire, M., 2009. Patterns in pCO2 in boreal streams and rivers of northern Quebec, Canada. Global Biogeochemical Cycles, 23(2).

Tóth, J. and Almási, I., 2001. Interpretation of observed fluid potential patterns in a deep sedimentary basin under tectonic compression: Hungarian Great Plain, Pannonian Basin. Geofluids, 1(1), 11–36.

Vaghefi, S.A., Keykhai, M., Jahanbakhshi, F., Sheikholeslami, J., Ahmadi, A., Yang, H. and Abbaspour, K.C., 2019. The future of extreme climate in Iran. Scientific reports, 9(1), 1464.

Veysey, J., Fouke, B.W., Kandianis, M.T., Schickel, T.J., Johnson, R.W. and Goldenfeld, N., 2008. Reconstruction of water temperature, pH, and flux of ancient hot springs from travertine depositional facies. Journal of Sedimentary Research, 78(2), 69–76.

Vignaroli, G., Berardi, G., Billi, A., Kele, S., Rossetti, F., Soligo, M. and Bernasconi, S.M., 2016. Tectonics, hydrothermalism, and paleoclimate recorded by Quaternary travertines and their spatio-temporal distribution in the Albegna basin, central Italy: Insights on Tyrrhenian margin neotectonics. Lithosphere, 8(4), 335–358.

Wang, S., Pang, Z., Liu, J., Lin, P., Liu, S. and Yin, M., 2013. Origin and evolution characteristics of geothermal water in the Niutuozhen geothermal field, North China Plain. Journal of Earth Science, 24(6), 891–902.

Yang, P., Cheng, Q., Xie, S., Wang, J., Chang, L., Yu, Q., Zhan, Z. and Chen, F., 2017. Hydrogeochemistry and geothermometry of deep thermal water in the carbonate formation in the main urban area of Chongqing, China. Journal of Hydrology, 549, 50–61.

Yang, P., Luo, D., Hong, A., Ham, B., Xie, S., Ming, X., Wang, Z. and Pang, Z., 2019. Hydrogeochemistry and geothermometry of the carbonate-evaporite aquifers controlled by deep-seated faults using major ions and environmental isotopes. Journal of Hydrology, 579, 124116.

Yousefi, H., Noorollahi, Y., Ehara, S., Itoi, R., Yousefi, A., Fujimitsu, Y., Nishijima, J. and Sasaki, K., 2010. Developing the geothermal resources map of Iran. Geothermics, 39(2), 140–151.

Figure captions

Table captions